PHOTONICS Research

Optically induced rotation of Rayleigh particles by arbitrary photonic spin

Guanghao Rui,[1] Ying Li,[1] Sichao Zhou,[2] Yusong Wang,[1] Bing Gu,[1] Yiping Cui,[1,4] and Qiwen Zhan[2,3,5]

[1]Advanced Photonics Center, Southeast University, Nanjing 210096, China
[2]Department of Electro-Optics and Photonics, University of Dayton, Dayton, Ohio 45469, USA
[3]School of Optical-Electrical and Computer Engineering, University of Shanghai for Science and Technology, Shanghai 200093, China
[4]e-mail: cyp@seu.edu.cn
[5]e-mail: qzhan1@udayton.edu

Received 6 August 2018; revised 31 October 2018; accepted 31 October 2018; posted 2 November 2018 (Doc. ID 341017); published 20 December 2018

Optical trapping techniques hold great interest for their advantages that enable direct handling of nanoparticles. In this work, we study the optical trapping effects of a diffraction-limited focal field possessing an arbitrary photonic spin and propose a convenient method to manipulate the movement behavior of the trapped nanoparticles. In order to achieve controllable spin axis orientation and ellipticity of the tightly focused beam in three dimensions, an efficient method to analytically calculate and experimentally generate complex optical fields at the pupil plane of a high numerical aperture lens is developed. By numerically calculating the optical forces and torques of Rayleigh particles with spherical/ellipsoidal shape, we demonstrate that the interactions between the tunable photonic spin and nanoparticles lead to not only 3D trapping but also precise control of the nanoparticles' movements in terms of stable orientation, rotational orientation, and rotation frequency. This versatile trapping method may open up new avenues for optical trapping and their applications in various scientific fields.

https://doi.org/10.1364/PRJ.7.000069

1. INTRODUCTION

In 1986, Ashkin and his colleagues reported the first observation of stable optical trapping of microparticles, which was created by the optical force from a single laser beam [1]. Due to noncontact and nondestructive features, optical tweezers has exceeded mechanical force in many applications ranging from physics to biochemistry [2–4]. Besides, it also provides an all-optical method that makes it possible to manipulate particles ranging in size from tens of nanometers to micrometers [5–7]. Generally, a particle is trapped by the gradient force in the high-intensity region surrounding the focal point of a tightly focused Gaussian beam, where the locally harmonic and conservative optical force field allows the elastic energy of the trap to be equated with the thermal energy and other external force contributions (such as gravity or drag force). In addition, the movement behavior of the trapped particle can be controlled by the torque, which arises from the transfer of angular momentum. For example, Padgett and coworkers used a circularly polarized Laguerre–Gaussian beam with a large value of topological charge, thereby producing an annular beam of a diameter significantly larger than that of the particle [8]. In such situations, rather than the particle being trapped on the beam axis, the gradient force confines the particle to the high-intensity annular ring. This configuration of optical spanner reveals a difference in the behavior between orbital and spin angular momentum (SAM). While the transfer of SAM causes a particle to spin around its own axis, the transfer of orbital angular momentum causes a particle to orbit around the beam's axis. Besides, the optical spin-to-orbital angular momentum conversion is also demonstrated to alter the orbital rotation speed of trapped particles, which are highly desirable in micromechanical measurement and microsystems [9]. With the rapid development of optical engineering technology, substantial effort has been devoted to shaping the optical field and thereby the novel force field, leading to the growing theme in optical micro-manipulation. Tailoring the incident wave field and beam profile to enhance or reduce light scattering from a particle can create a paradigm shift in optical manipulation procedures, such that negative pulling or positive pushing forces can be generated and used to advantage depending on the application in mind [10–14].

Besides using sculpted light fields to control tiny objects, the concept of shaping an object rather than the light field also has attracted increasing attention, which promises to propel light–matter research in an exciting novel direction [15,16]. In recent years, there has been substantial interest in the optical trapping

behavior of spheroidal particles [17–20], which are formed by a single deformation of a sphere and can be seen as being representative of elongated or flattened particles such as, for example, red blood cells, chloroplasts, and phospholipid vesicles [21–23]. Compared with spherical particles, particles with a nonspherical shape exhibit unique proprieties. It has been demonstrated both theoretically and experimentally that a spheroid with a prolate/oblate shape would align its symmetry axis with/perpendicular to the beam axis, in which case the overlap between the interior of the spheroid and the incident intensity can be maximized [24]. Besides, the orientation of the spheroid is also determined by the electric polarization torque. For example, trapping properties of Rayleigh spheroids in a light field with different states of polarization (SOPs) are investigated [12,13]. However, previous works studying the interaction between circular polarization and nanoparticles only address optical fields with longitudinal SAM with its spin orientation along the optical axis. It has been reported that a nondiffraction-limited focused beam with purely transverse angular momentum is demonstrated by tight focusing of a polarization tailored vector beam [25], leading to promising applications in optical trapping and manipulation.

The aim of this work is to investigate the optical trapping effects of an arbitrary photonic spin and propose an efficient method to manipulate the movement behaviors of nanoparticles. Although controllable photonic spin orientation within an optical focal field has been reported, spin axis orientation in a specific plane can only be achieved [26]. In this work, we demonstrate an effective method to generate arbitrary spin axis orientation of a tightly focused beam in three dimensions. Considering the orientation and the ellipticity of the photonic spin within the trapping light, the optical force and intrinsic torque exerted on the nanoparticle with a spherical/ellipsoidal shape and different spatial orientations are theoretically calculated. The interactions between the tunable photonic spin and the nanoparticles enable not only the 3D trapping but also the precise control of the nanoparticle in terms of its stable orientation, rotational orientation, and rotation frequency.

2. GENERATION OF ARBITRARY PHOTONIC SPIN IN THREE DIMENSIONS

Considering a focal field with arbitrary spin in 3D space, the direction vector of the spin axis is (cos α, cos β, cos γ), where α, β, and γ are the angles between the spin axis of the focal field and the positive direction of the x, y, and z axes. This photonic spin can be synthesized by two electric dipoles (dipole A and B) with phase difference of $\Delta\phi$ and strength ratio of η, which are located at the focal point of a high numerical aperture (NA) lens (shown in Fig. 1). The oscillation direction of dipole A is in the y–z plane and has an angle of θ_A [$\theta_A = \arctan(\cos\gamma/\cos\beta)$] with respect to the negative direction of the z axis. Dipole B can be further decomposed into two subdipoles (dipole B_1 and dipole B_2). Dipole B_1 is along the x axis with strength of N_1, while dipole B_2 oscillates in the y–z plane with strength of N_2 and has an angle of θ_B ($\theta_B = \pi/2 + \theta_A$) with respect to the negative direction of the z axis. There is no phase difference between these two subdipoles, and the relative strength depends on the orientation of the photonic spin:

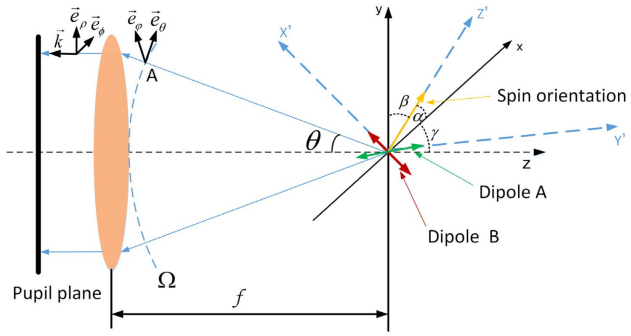

Fig. 1. Calculation of the pupil field to obtain a focused beam with arbitrary photonic spin orientation through coherent superposition of the radiation patterns from electric dipoles.

$$N_1 = \frac{\cos^2\beta + \cos^2\gamma}{\sqrt{(\cos^2\beta + \cos^2\gamma)^2 + (\cos\alpha\cos\beta)^2 + (\cos\alpha\cos\gamma)^2}},$$
$$N_2 = \frac{\sqrt{(\cos\alpha\cos\beta)^2 + (\cos\alpha\cos\gamma)^2}}{\sqrt{(\cos^2\beta + \cos^2\gamma)^2 + (\cos\alpha\cos\beta)^2 + (\cos\alpha\cos\gamma)^2}}. \quad (1)$$

In order to generate a focal field with a predetermined photonic spin, the input field must be deduced through reversing the radiation patterns from these dipoles, which are collected and collimated by the lens to form the field distribution in the pupil plane. According to the dipole antenna theory [27], the electric radiation on the spherical surface Ω can be written as the linear combination of the radiation pattern from these three dipoles. Considering the projection function of the objective lens with the sine condition, the required incident pupil field can be found to be

$$\begin{aligned} E(r,\varphi) &= \frac{1}{\sqrt{\cos\theta}}(A\cdot\vec{e}_x + B\cdot\vec{e}_y),\\ A &= \eta e^{i\Delta\phi}(\cos\theta_A\sin\theta\cos\varphi - \sin\theta_A\cos\theta\sin\varphi\cos\varphi\\ &\quad + \sin\theta_A\cos\varphi\sin\varphi) + N_1(-\cos\theta\cos^2\varphi - \sin^2\varphi)\\ &\quad + N_2(\cos\theta_B\sin\theta\cos\varphi - \sin\theta_B\cos\theta\sin\varphi\cos\varphi\\ &\quad + \sin\theta_B\cos\varphi\sin\varphi),\\ B &= \eta e^{i\Delta\phi}(\cos\theta_A\sin\theta\sin\varphi - \sin\theta_A\cos\theta\sin^2\varphi\\ &\quad - \sin\theta_A\cos^2\varphi) + N_1(-\cos\theta\cos\varphi\sin\varphi + \sin\varphi\cos\varphi)\\ &\quad + N_2(\cos\theta_B\sin\theta\sin\varphi - \sin\theta_B\cos\theta\sin^2\varphi\\ &\quad - \sin\theta_B\cos^2\varphi), \end{aligned} \quad (2)$$

where $r = f\cdot\sin\theta$, φ is the azimuthal angle, and $\vec{e}_x$ and $\vec{e}_y$ are the unit vectors along the x and y axes, respectively. After being focused by the high NA lens, the electric field in the vicinity of the focus can be calculated by using Richard–Wolf vectorial diffraction theory and expressed as [28]

$$\vec{E}(r_p,\phi,z_p) = \frac{i}{\lambda}\int_0^{\theta_{\max}}\int_0^{2\pi}(X\cdot\vec{e}_x + Y\cdot\vec{e}_y + Z\cdot\vec{e}_z) \times e^{jkr_p\sin\theta\cos(\varphi-\phi)+jz_p\cos\theta}\sin\theta\,d\theta\,d\varphi, \quad (3)$$

where λ is the optical wavelength of the illumination, $\theta_{\max}$ is the maximal focusing angle determined by the NA of the lens, and $r_p = (x^2+y^2)^{1/2}$ and $\phi = \arctan(y/x)$ are the polar

coordinates in the focal volume. X, Y, and Z are the field components that can be expressed as

$$
\begin{aligned}
X = {} & \eta e^{i\Delta\phi}(\cos\theta_A \sin\theta\cos\theta\cos\varphi - \sin\theta_A\cos^2\theta\cos\varphi\sin\varphi \\
& + \sin\theta_A\cos\varphi\sin\varphi) + [N_1(-\cos^2\theta\cos^2\varphi - \sin^2\varphi) \\
& - N_2(\cos\theta_B\sin\theta\cos\theta\cos\varphi - \sin\theta_B\cos^2\theta\cos\varphi\sin\varphi \\
& + \sin\theta_B\cos\varphi\sin\varphi)], \\
Y = {} & \eta e^{i\Delta\phi}(\cos\theta_A\sin\theta\cos\theta\sin\varphi - \sin\theta_A\cos^2\theta\sin^2\varphi \\
& - \sin\theta_A\cos^2\varphi) + [N_1(\sin^2\theta\sin\varphi\cos\varphi) \\
& - N_2(\cos\theta_B\sin\theta\cos\theta\sin\varphi \\
& - \sin\theta_B\cos^2\theta\sin^2\varphi - \sin\theta_B\cos^2\varphi)], \\
Z = {} & \eta e^{i\Delta\phi}(\cos\theta_A\sin^2\theta - \sin\theta_A\cos\theta\sin\theta\sin\varphi) \\
& + [N_1(-\cos\theta\sin\theta\cos\varphi) \\
& - N_2(\cos\theta_B\sin^2\theta - \sin\theta_B\cos\theta\sin\theta\sin\varphi)]. \qquad (4)
\end{aligned}
$$

The feasibility of the proposed strategy is first demonstrated by generating a circularly polarized focal field with its spin axis along $(\alpha, \beta, \gamma) = (60°, 60°, 45°)$. Figures 2(a) and 2(b) show the corresponding spatial distribution of the input light in terms of both intensity and polarization, which is calculated by Eq. (2) with $(\Delta\phi, \eta) = (\pi/2, 1)$. The SOP at the beam cross-section is indicated by the polarization ellipses, where green and blue colors represent left- and right-handedness, respectively. It can be clearly seen that the amplitude and the polarization distributions of the illumination are nonuniform. Most of the input light is in the right-handed polarization with different ellipticity, and the intensity is much stronger around the lower-left corner. As the statistical data of the illumination pattern summarized in Fig. 2(b), the histogram of the ellipticity peaks around $[0.175\pi, 0.225\pi]$. To explore the focusing properties of this optical complex field, the electric field of the focal field near the focus of an objective lens with a NA of 0.95 is calculated by Eq. (3) and shown in Fig. 3(a). Both the intensity and the polarization distributions are projected to three orthogonal planes in

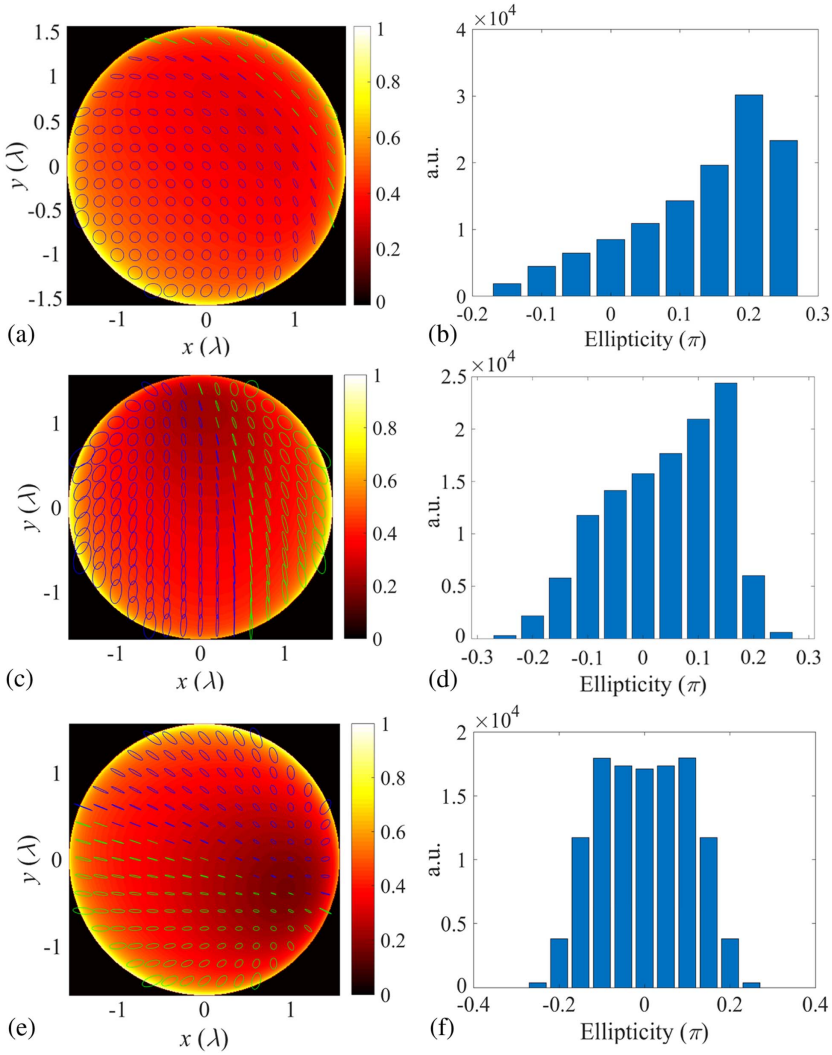

Fig. 2. (a), (c), and (e) Intensity distribution superimposed with polarization map. (b), (d), and (f) Histogram of ellipticity of the ideal incident pupil field for generating (a) photonic spin orientated along $(\alpha, \beta, \gamma) = (60°, 60°, 45°)$, (c) photonic spin with ellipticity of 2 and orientation along $(\alpha, \beta, \gamma) = (20°, 80°, 73°)$, and (e) photonic spin with elevation angle of −45° and orientation along $(\alpha, \beta, \gamma) = (110°, 20°, 90°)$.

the x'–y'–z' coordinate, in which the z' axis coincides with the direction of the photonic spin, and the x'–y' plane containing the origin point is perpendicular to the spin axis. The full width at half-maximum along the x', y', and z' axes is measured to be 0.55λ, 0.56λ, and 1.30λ, leading to the focal volume of $0.21\lambda^3$, which is smaller than the diffraction limited focal volume of $0.3\lambda^3$ [29]. From the polarization ellipses, one can find that the ellipticity within the main lobe is close to 1 in the x'–y' plane and 0 in the x'–z' and y'–z' planes, indicating the circular polarization with spin along the z' axis. To better study the polarization characteristics of the focal field, the full Stokes parameters in the x'–y' plane are calculated and illustrated in Figs. 3(b)–3(d). It can be seen that the values of the S_3 image are nearly a unit in the main lobe, indicating the right-hand circular polarization. Besides, the direction angles of the spin axis can also be visualized by the spin density $\vec{S}$, which is expressed as the imaginary part of the electric field cross product [30],

$$\vec{S} \propto \mathrm{Im}\{\vec{E}^* \times \vec{E}\}, \tag{5}$$

where $\vec{E}$ is the incident electric field, the superscript * denotes the conjugate of a complex number, and $\mathrm{Im}\{\cdot\}$ is the imaginary part of a complex number. Figures 3(e)–3(g) show the spin density of the focused beam calculated by the electric field in the x'–y'–z' coordinate. It can be seen that the z' component of the normalized spin density is much stronger than the x' and y' components in the main lobe. Consequently, the spin axis of the focused beam is mainly in the negative z' axis, namely, the orientation of the photonic spin is along $(\alpha, \beta, \gamma) = (60°, 60°, 45°)$.

In addition to creating photonic spin with arbitrary orientation, it is also feasible to generate a focal field with controllable ellipticity and elevation angle, which can be realized by adjusting $\Delta\phi$ and η. For example, the ideal input field distribution with a polarization map and ellipticity histogram for synthesizing an elliptical polarized focal field with ellipticity of 2 and elevation angle of 45° is shown in Figs. 2(c) and 2(d) and Figs. 2(e) and 2(f), in which cases the parameters $(\alpha, \beta, \gamma, \Delta\phi, \eta)$ are chosen to be (20°, 80°, 73°, $\pi/2$, 2) and (110°, 20°, 90°, $-\pi/4$, 1). Note that the ellipticity peaks around $[0.125\pi, 0.175\pi]$ and $[-0.125\pi, 0.125\pi]$, respectively. Figures 4(a) and 5(a) show the projection of the intensity and SOP distribution of the focused beam by a lens with a NA of 0.95. Compared with the case presented in Fig. 3(a), although the shape of the focal field does not change significantly, the SOP distribution of the main lobe in the x'–y' plane is consistent with the theoretical predications. These features can be more clearly revealed by the Stokes image [shown in Figs. 4(b)–4(d) and Figs. 5(b)–5(d)] and the spin density distribution [shown in Figs. 4(e)–4(g) and Figs. 5(e)–5(g)]. As shown in Fig. 4, the main lobe possesses nonzero S_1 and positive S_3, indicating the right-hand elliptical polarization with its major axis along the x' axis. Besides, the peak locations of S_1

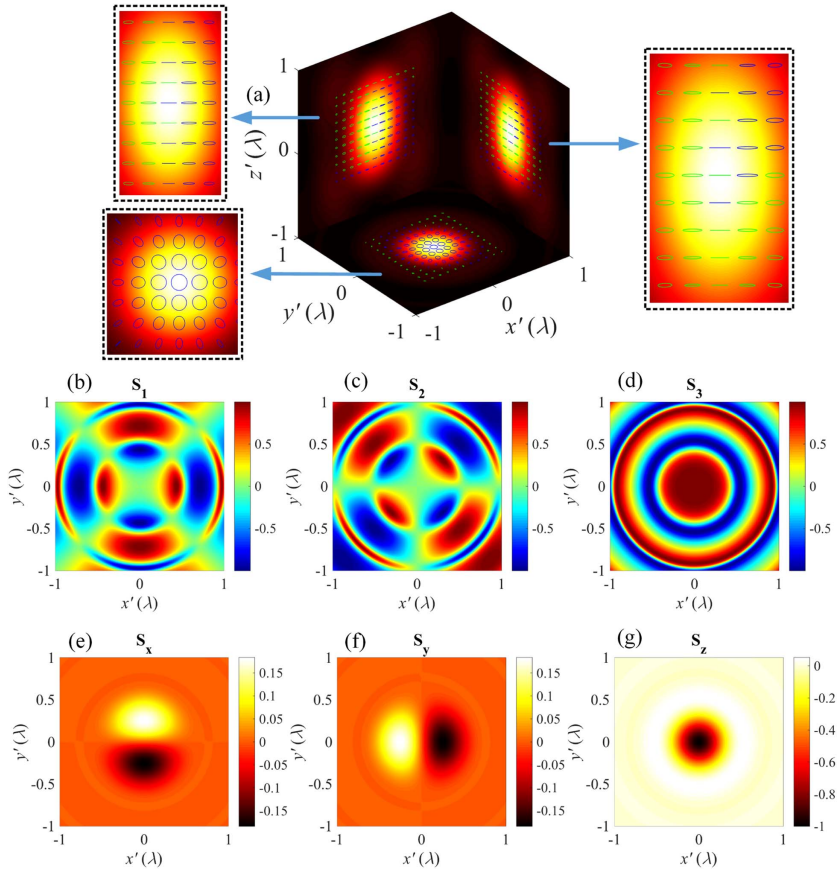

Fig. 3. (a) Normalized intensity distribution. (b)–(d) Stokes images. (e)–(g) Spin density distribution in the vicinity of the focus of the highly focused light given in Fig. 2(a).

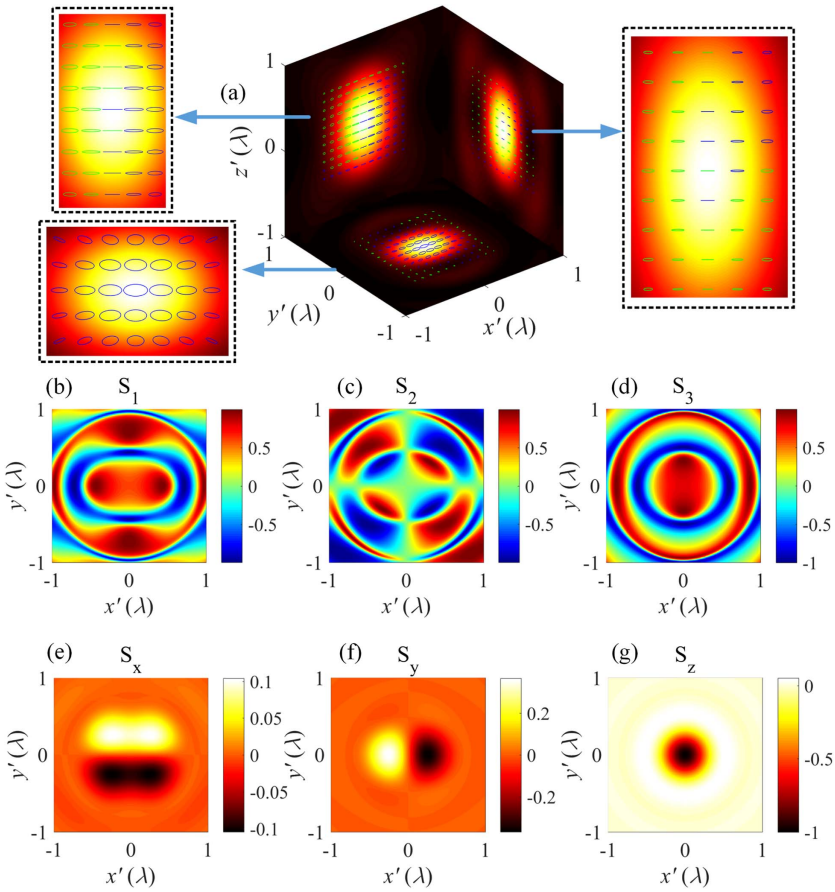

Fig. 4. (a) Normalized intensity. (b)–(d) Stokes images. (e)–(g) Spin density distribution in the vicinity of the focus of the highly focused light given in Fig. 2(c).

and negative S_3 within the main lobe presented in Fig. 5 indicate the generation of elliptical polarization with left-handedness and an elevation angle of 45°.

In the experiment, a vectorial optical field generator (VOF-Gen) is adopted to create an arbitrary optical field with independent control of phase, amplitude, and polarization distribution on the pixel level [31]. A diagram of the experiment setup is illustrated in Fig. 6. A collimated linearly polarized He–Ne laser is used as the light source. Taking advantage of the HDTV format of the Holoeye HEO 1080P reflective phase-only liquid crystal spatial light modulator (SLM), each SLM panel is divided into two halves, and each half of the SLM panels is used to realize the control of one degree of freedom, thus enabling full control of all the degrees of freedom to create an arbitrary complex optical field. The engineered optical field can be directly observed on a CCD camera (Spiricon SP620U). The experimental results of the input beam designed for generating circularly polarized photonic spin with orientation $(\alpha, \beta, \gamma) = (60°, 60°, 45°)$ are shown in Fig. 7(a). The full Stokes parameter measurement is performed to reveal the spatial distribution of the SOP of the generated beam. In order to enhance the visibility of the polarization ellipse, polarization with right-handedness is represented by yellow. As shown in Fig. 7(b), the histogram of the ellipticity peak around $[0.175\pi, 0.225\pi]$ demonstrates the generation of the designed SOP distribution, as presented in Fig. 2(a). To validate the versatility of the proposed method, the optical fields presented in Figs. 2(c) and 2(e) are also experimentally generated and shown in Figs. 7(c) and 7(e). The corresponding ellipticity peaks around $[0.075\pi, 0.215\pi]$ and $[-0.075\pi, 0.075\pi]$, respectively [shown in Figs. 7(d) and 7(f)].

In order to quantitatively evaluate the synthesized input light in terms of the overall quality of the SOP, the cumulative normalized Stokes parameters are introduced:

$$P_i = \sqrt{\frac{\sum S_i^2(x_0, y_0)}{\sum S_0^2(x_0, y_0)}}, \qquad i = 1, 2, 3, \tag{6}$$

where (x_0, y_0) are the indexes of the pixels of the Stokes image. Table 1 shows the theoretical and experimental values of P_1, P_2, and P_3 of the input light presented in Figs. 2 and 7. The average error is calculated to be only about 4%, showing good agreement between the theoretical design and the experimental results. Consequently, we demonstrate that the VOF-Gen is capable of tailoring the complex light field with high quality, which is necessary to synthesize a controllable photonic spin in 3D space.

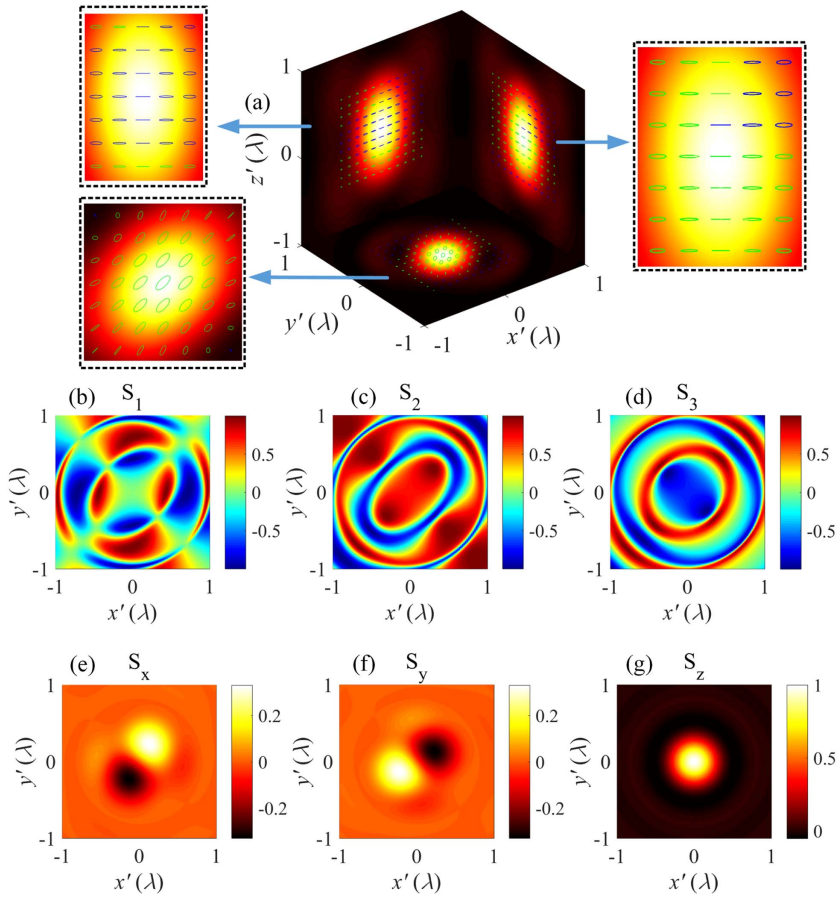

Fig. 5. (a) Normalized intensity. (b)–(d) Stokes images. (e)–(g) Spin density distribution in the vicinity of the focus of the highly focused light given in Fig. 2(e).

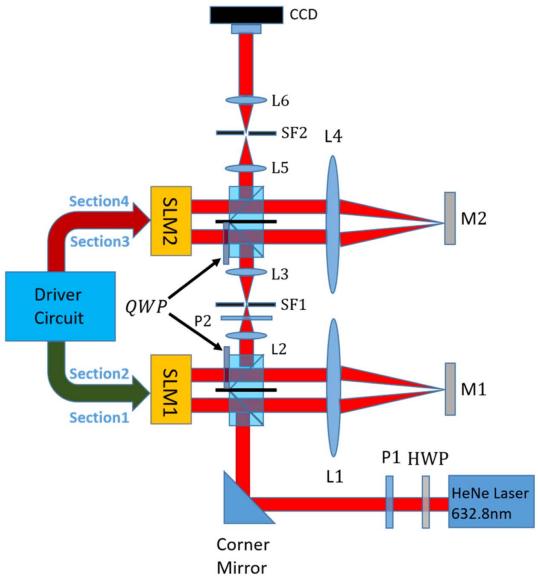

Fig. 6. Diagram of the experimental setup. HWP, half-wave plate; P, polarizer; BS, beam splitter; L, lens; M, mirror; SF, spatial filter.

3. OPTICAL FORCE AND TORQUE UNDER DIPOLE APPROXIMATION

Considering an ellipsoidal particle that is much smaller than the incident wavelength, it can be treated in the quasi-static limit and represented by point polarizability. Different from a spherical particle, the polarizability of an ellipsoidal particle is not a scalar but a tensor of rank two. The resulting force on a point electric polarizability is given by [32]

$$\vec{F} = \frac{1}{2}\,\mathrm{Re}\{\vec{p}(\nabla \times \vec{E}^{*})\}, \tag{7}$$

where $\vec{p} = \alpha\vec{E}$ is the electric dipole moment and α is the electric polarizability. $\mathrm{Re}\{\cdot\}$ is the real part of a complex number. The modified electric polarizability can be expressed as [33]

$$\alpha = \frac{\alpha_0}{1 - i\alpha_0 k^3/(6\pi)}, \tag{8}$$

where α_0 is a matrix representing Claussius–Mossotti polarizability,

$$\alpha_0 = \begin{pmatrix} \alpha_{0x'} & 0 & 0 \\ 0 & \alpha_{0y'} & 0 \\ 0 & 0 & \alpha_{0z'} \end{pmatrix}. \tag{9}$$

The coefficients $\alpha_{0,i}$ represent the components of the polarizability tensor,

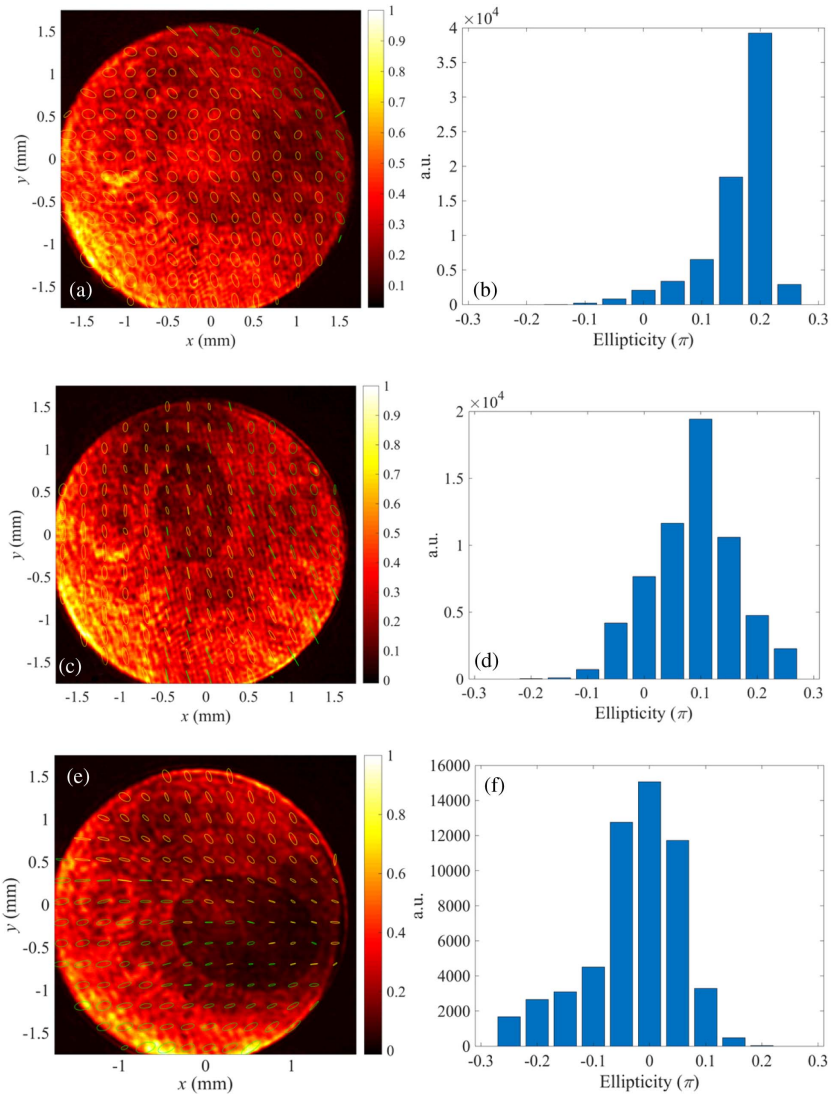

Fig. 7. Experimental results of the (a), (c), and (e) intensity distribution with polarization map and (b), (d), and (f) histogram of ellipticity corresponding to the incident pupil field presented in Figs. 2(a), 2(c), and 2(e), respectively.

$$\alpha_{0,i} = \frac{1}{3}abc\frac{\varepsilon_m(\omega)/\varepsilon - 1}{1 + [\varepsilon_m(\omega)/\varepsilon - 1]n_i}, \qquad (i = a, b, c), \tag{10}$$

where n_i is the depolarizing factor [34],

$$\begin{aligned} n_i &= \frac{1}{2}abc\int_0^\infty [(s+a^2)^2(s+b^2)(s+c^2)]^{-1}\mathrm{d}s, \qquad (i = x') \\ &= \frac{1}{2}abc\int_0^\infty [(s+a^2)(s+b^2)^2(s+c^2)]^{-1}\mathrm{d}s, \qquad (i = y') \\ &= \frac{1}{2}abc\int_0^\infty [(s+a^2)(s+b^2)(s+c^2)^2]^{-1}\mathrm{d}s, \qquad (i = z'), \end{aligned} \tag{11}$$

where k is the wave vector, and $\varepsilon_m(\omega)$ and ε are the relative permittivity of the particle from bulk material and the surrounding medium, respectively. Parameters a, b, and c are half the length of the principal axes, corresponding to the semimajor and semiminor axes of an ellipse.

The orientation of the ellipsoid, with respect to its center of mass, can be described by two angular momenta (Θ_0, Φ_0), where Θ_0 and Φ_0 are the polar and azimuthal angles of the major axis, respectively (shown in Fig. 8). It is known that the polarizability tensor of the particle would be affected by its orientation in space as $\alpha_{0,ij} = R_{i\delta}\alpha_{0,\delta\gamma}R^{-1}_{\gamma j}$, where the rotation matrix R_{ij} is given by Refs. [17,18,35] as

Table 1. Theoretical and Experimental P_i Values for the Incident Light Presented in Figs. 2 and 7

	$(\alpha,\beta,\gamma,\Delta\phi,\eta) = (60°, 60°, 45°, \pi/2, 1)$			$(\alpha,\beta,\gamma,\Delta\phi,\eta) = (20°, 80°, 73°, \pi/2, 2)$			$(\alpha,\beta,\gamma,\Delta\phi,\eta) = (110°, 20°, 90°, -\pi/4, 1)$		
	P_1	P_2	P_3	P_1	P_2	P_3	P_1	P_2	P_3
Theory	0.35	0.38	0.86	0.52	0.43	0.74	0.61	0.56	0.56
Experiment	0.34	0.40	0.83	0.54	0.40	0.72	0.63	0.55	0.54

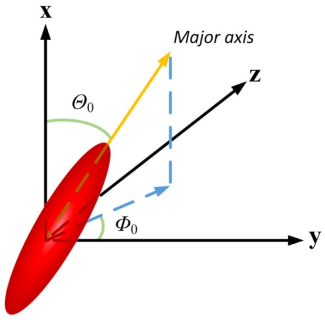

Fig. 8. Spatial orientation of the spheroid.

$$R_{ij} = \begin{pmatrix} \cos\theta_0 \cos\phi_0 & -\sin\phi_0 & \sin\theta_0 \cos\phi_0 \\ \cos\theta_0 \sin\phi_0 & \cos\phi_0 & \sin\theta_0 \sin\phi_0 \\ -\sin\theta_0 & 0 & \cos\theta_0 \end{pmatrix}. \quad (12)$$

Assuming a particle immersed in the focal volume of a highly focused optical field, its movement is subject to the induced time-averaged optical force, which arises from the transfer of the linear momentum between light and matter. In the case of light carrying a vortex phase front, the particle would experience a longitudinal orbital torque, leading to orbiting around the optical axis. Furthermore, the particle would also spin around its center of mass due to the transfer of the SAM from the light. This intrinsic torque $\vec{\Gamma}$ can be expressed as [17,18,32,36]

$$\vec{\Gamma} = \frac{1}{2}|\alpha|^2 \Re\left\{\frac{1}{\alpha_0^*}(\vec{E} \times \vec{E}^*)\right\}. \quad (13)$$

Without loss of generality, a spheroidal particle with size $(a, b, c) = (30\ \text{nm}, 30\ \text{nm}, 50\ \text{nm})$ and refractive index of 1.59 is placed near the focus of the photonic spin presented in Fig. 3(a). In addition, the imaging space of the objective lens is filled with water (refractive index of 1.33); further, the wavelength and the power of the trapping laser are assumed to be 1064 nm and 100 mW.

First, we assume the initial orientation of the spheroid is $(\Theta_0 = 45°, \Phi_0 = 45°)$. The distribution of the optical force in the local coordinate is calculated with Eq. (7) and shown in Fig. 9. It can be clearly seen that the particle would be

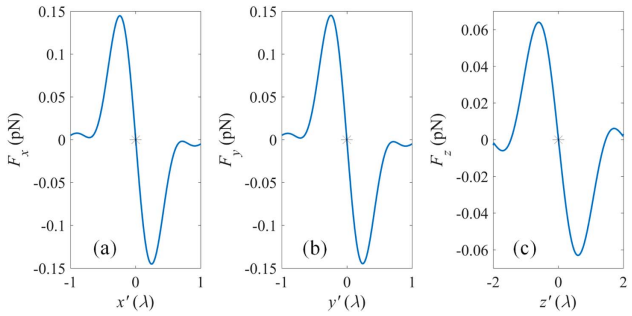

Fig. 9. Optical force on the dielectric spheroidal particle located near the focus of the photonic spin presented in Fig. 3(a). Equilibrium position is indicated by the asterisk.

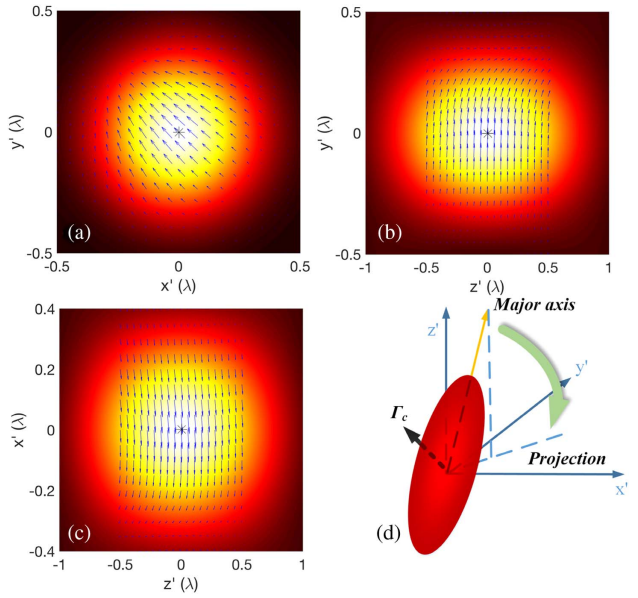

Fig. 10. Distribution of the optical torque in the (a) x'–y', (b) y'–z', and (c) x'–z' planes. (d) Corresponding rotation diagram of a spheroid with orientation at $(\Theta_0 = 45°, \Phi_0 = 45°)$. Equilibrium position is indicated by the asterisk.

trapped at the origin. The stability of the optical trapping can be demonstrated by the potential depth of $10k_BT$ at the equilibrium position [37], where k_B is the Boltzmann constant and temperature T is taken to be 20°C. Furthermore, the optical torque distribution and the corresponding 3D view of the torque vector on the spheroid are also plotted in Fig. 10. The position of the particle is marked by the asterisk. One can find that $\Gamma_{z'}$ is much smaller than the torque in the x'–y' plane. The direction of the torque vector is calculated to be (135°, 46°, 84°) with respect to the x', y', and z' axes. From Fig. 10(d), it can be seen that the torque tends to rotate the major axis of the spheroid with increasing Θ_0. To study the dynamics of the rotating particle, Fig. 11(a) shows the torque at the equilibrium position for different values of Θ_0 with fixed $\Phi_0 = 45°$. The axial $\Gamma_{z'}$ is kept negligible for circular polarization regardless of the spatial orientation of the spheroid. Besides, it can be seen that the major axis of the spheroid would be rotated to be parallel to the projection of the major axis in the x'–y' plane. Figure 11(b) represents the relationship between the torque and Φ_0 with fixed $\Theta_0 = 45°$. Note that the magnitude of the torque in the x'–y' plane is independent with the azimuthal angle Φ_0, while the direction of the torque is determined by Φ_0. Note that the torque is perpendicular to the plane containing the major axis of the spheroid and the spin axis of the focal field. Consequently, the stable orientation of the spheroid can be adjusted by the orientation of the photonic spin, which can be realized by the technique proposed in Section 2.

Different from the spheroid, the dielectric spherical nanoparticle would not be rotated by the optical field because there is no stable orientation due to the symmetric shape. However, from Eq. (13) one can find that nonzero intrinsic torque is obtainable even for a spherical nanoparticle if the particle is absorptive and the optical field is not locally linearly polarized.

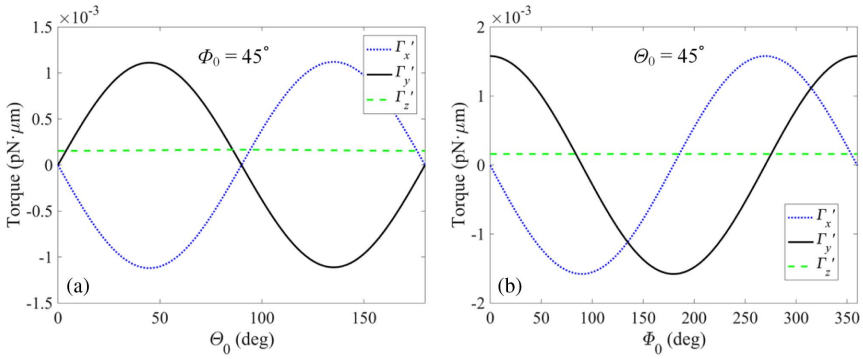

Fig. 11. Torque exerted on the spheroid at the equilibrium position versus (a) the polar angle Θ_0 and (b) the azimuthal angle Φ_0.

Assuming an absorptive nanoparticle with refractive index of $1.59 + 0.01i$ and radius of 50 nm is placed near the focus of the focal field given in Fig. 3(a), then to better understand the physical mechanism of the optical force, Eq. (7) is rewritten as [38]

$$\vec{F} = \frac{1}{4}\varepsilon_0 \mathrm{Re}\{\alpha\}\nabla|\vec{E}|^2 + \frac{n\sigma}{c}\langle \vec{S}_v \rangle - \frac{\varepsilon_0 \sigma}{2k_0}\mathrm{Im}\left\{(\vec{E}\cdot\nabla)\vec{E}^*\right\}, \quad \textbf{(14)}$$

where ε_0 is the vacuum permittivity, c is the speed of light, $\vec{S}_v$ is the Poynting vector, and $\sigma = k\,\mathrm{Im}\{\alpha\}$ is the total cross section of the particle. In Eq. (14), the first term is the gradient force proportional to the gradient of the intensity of the focal field. The second term is identified as the radiation pressure force proportional to the Poynting vector, and the third term is a force arising from the presence of spatial polarization gradients. The combination of the second and the third terms gives the scattering force. The optical force exerted on the spherical particle is calculated with Eq. (14) and illustrated in Fig. 12. It can be clearly seen that the gradient force dominates in the x'–y' plane, which would confine the particle at the center of the focus.

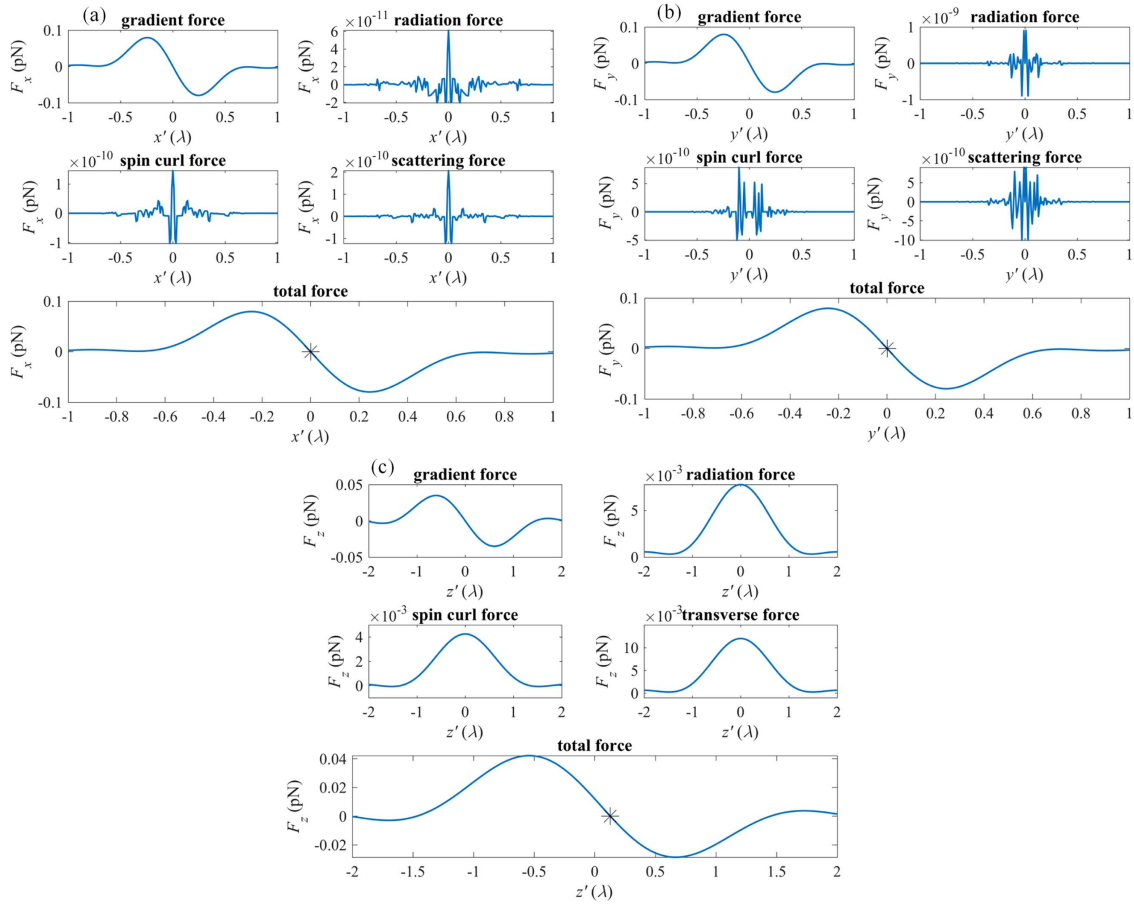

Fig. 12. Optical force along (a) x', (b) y', and (c) z' axes exerted on the 50 nm absorbing nanoparticle located near the focus of the photonic spin presented in Fig. 3(a). Equilibrium position is indicated by the asterisk.

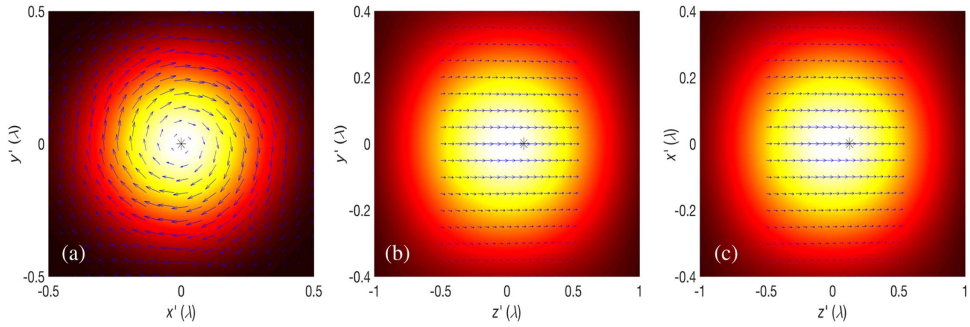

Fig. 13. Distribution of the optical torque in the (a) x'–y', (b) y'–z', and (c) x'–z' planes for absorbing spherical nanoparticle. The equilibrium position is indicated by the asterisk.

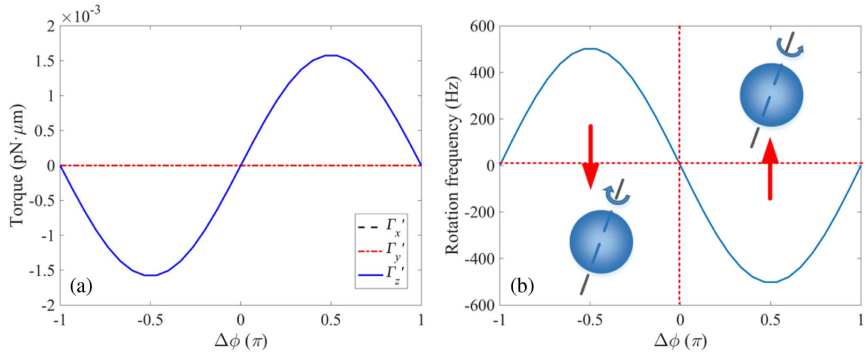

Fig. 14. Particle rotation as a result of the torque from elliptically polarized light. (a) Torque and (b) rotation frequency for absorbing nanoparticles are shown as a function of $\Delta\phi$, the phase difference that determines the ellipticity of the focal field.

However, the radiation force is not negligible along the z' axis due to the strong scattering form of the absorptive particle; therefore, the axial equilibrium position is shifted to 0.13λ. The corresponding potential depth is calculated to be $6k_BT$. As shown in Fig. 13, the spherical particle would experience pure torque along the z' direction at the equilibrium position, leading to the rotation of the particle along the spin axis. Consequently, it is feasible to tune the rotation axis of the spherical particle, which is realized by adjusting the orientation of the photonic spin. Furthermore, the relationship between the torque and the ellipticity of the focal field is studied and illustrated in Fig. 14(a). In this case, strength ratio η is fixed to 1, and different phase difference $\Delta\phi$ is considered, leading to the focal field with different ellipticity and handedness. It can be seen that the rotation direction of the particle is determined by the handedness of the ellipticity. Besides, the decrease of the ellipticity could result in decreased intrinsic torque. For a particle that has the drag torque of Γ in a medium of viscosity ξ, the rotating frequency Ω_p is given by $\Omega_p = \Gamma/(-8\pi\xi r^3)$ [39–41], where r is the radius of the particle, and ξ is the viscosity of water (about 0.001 $\mathrm{N\cdot s/m^2}$ at 20°C). To quantify the effects of elliptically polarized light, the particle's rotation frequency is calculated, which we plot in Fig. 14(b), against the phase difference $\Delta\phi$. It confirms that the particle rotation is in fact a result of the torque from elliptically polarized light. Consequently, we can control the direction and rate of the particle's rotation by changing the orientation and the ellipticity of the photonic spin within the focal field.

4. CONCLUSION

In conclusion, we proposed a method to manipulate the movement behaviors of nanoparticles by using an arbitrary photonic spin in three dimensions. To achieve controllable spin axis orientation and ellipticity within a diffraction-limited tightly focused beam, the required pupil field is analytically derived through reversing the radiation patterns from three dipoles located at the focal point of a high NA lens and experimentally generated with a home-built VOF-Gen. Furthermore, the optical forces and intrinsic torques of a Rayleigh particle with a spherical or ellipsoidal shape and different spatial orientations trapped by tunable photonic spin were calculated. Numerical results demonstrate that the nanoparticles can be stably trapped near the focus. For ellipsoidal nanoparticles, the torque would align the major axis of the particle parallel to the projection of the major axis in the plane perpendicular to the photonic spin. For spherical nanoparticles, the torque would force the particle to rotate around the spin axis. Consequently, by tuning the spatial orientation of the photonic spin, it is feasible to control the stable and rotational orientations of nanoparticles. Besides, both the rotation direction and the rotation frequency can be adjusted by the ellipticity of the focal field. This versatile trapping method may open up new avenues for optical trapping and their applications in various scientific fields.

Funding. National Natural Science Foundation of China (NSFC) (11504049, 11474052, 11774055); Natural Science

Foundation of Jiangsu Province, China (BK20150593); National Key Basic Research Program of China (2015CB352002).

REFERENCES

1. A. Ashkin, J. M. Dziedzic, J. E. Bjorkholm, and S. Chu, "Observation of a single-beam gradient force optical trap for dielectric particles," Opt. Lett. **11**, 288–290 (1986).
2. M. A. El-Sayed, "Small is different: shape-, size-, and composition-dependent properties of some colloidal semiconductor nanocrystals," Acc. Chem. Res. **37**, 326–333 (2004).
3. M. A. El-Sayed, "Some interesting properties of metals confined in time and nanometer space of different shapes," Acc. Chem. Res. **34**, 257–264 (2001).
4. D. Gao, W. Ding, M. Nieto-Vesperinas, X. Ding, M. Rahman, T. Zhang, C. Lim, and C. Qiu, "Optical manipulation from the microscale to the nanoscale: fundamentals, advances and prospects," Light Sci. Appl. **6**, e17039 (2017).
5. D. G. Grier, "A revolution in optical manipulation," Nature **424**, 810–816 (2003).
6. A. N. Grigorenko, N. W. Roberts, M. R. Dickinson, and Y. Zhang, "Nanometric optical tweezers based on nanostructured substrates," Nat. Photonics **2**, 365–370 (2008).
7. K. C. Neuman and S. M. Block, "Optical trapping," Rev. Sci. Instrum. **75**, 2787–2809 (2004).
8. A. T. O'Neil, I. MacVicar, L. Allen, and M. J. Padgett, "Intrinsic and extrinsic nature of the orbital angular momentum of a light beam," Phys. Rev. Lett. **88**, 053601 (2002).
9. Y. Zhao, J. S. Edgar, G. D. M. Jeffries, D. McGloin, and D. T. Chiu, "Spin-to-orbital angular momentum conversion in a strongly focused optical beam," Phys. Rev. Lett. **99**, 073901 (2007).
10. J. Chen, J. Ng, Z. Lin, and C. T. Chan, "Optical pulling force," Nat. Photonics **5**, 531–534 (2011).
11. J. J. Sáenz, "Laser tractor beams," Nat. Photonics **5**, 514–515 (2011).
12. G. Rui and Q. Zhan, "Trapping of resonant metallic nanoparticles with engineered vectorial optical field," Nanophotonics **3**, 351–361 (2014).
13. G. Rui, X. Wang, B. Gu, Q. Zhan, and Y. Cui, "Manipulation metallic nanoparticle at resonant wavelength using engineered azimuthally polarized optical field," Opt. Express **24**, 7212–7223 (2016).
14. X. Wang, G. Rui, L. Gong, B. Gu, and Y. Cui, "Manipulation of resonant metallic nanoparticle using 4Pi focusing system," Opt. Express **24**, 24143–24152 (2016).
15. G. A. Swartzlander, Jr., T. J. Peterson, A. B. Artusio-Glimpse, and A. D. Raisanen, "Stable optical lift," Nat. Photonics **5**, 48–51 (2011).
16. J. Glückstad, "Sculpting the object," Nat. Photonics **5**, 7–8 (2011).
17. M. Li, S. Yan, B. Yao, M. Lei, Y. Yang, J. Min, and D. Dan, "Trapping of Rayleigh spheroidal particles by highly focused radially polarized beams," J. Opt. Soc. Am. B **32**, 468–472 (2015).
18. M. Li, S. Yan, B. Yao, Y. Liang, G. Han, and P. Zhang, "Optical trapping force and torque on spheroidal Rayleigh particles with arbitrary spatial orientations," J. Opt. Soc. Am. A **33**, 1341–1347 (2016).
19. S. H. Simpson and S. Hanna, "Computational study of the optical trapping of ellipsoidal particles," Phys. Rev. A **84**, 053808 (2011).
20. C. B. Chang, W.-X. Huang, K. H. Lee, and H. J. Sung, "Optical levitation of a non-spherical particle in a loosely focused Gaussian beam," Opt. Express **20**, 24068–24084 (2012).
21. J. Wu, Y. Li, D. Lu, Z. Liu, Z. Cheng, and L. He, "Measurement of the membrane elasticity of red blood cell with osmotic pressure by optical tweezers," Cryo Lett. **30**, 89–95 (2009).
22. S. Bayoudh, T. Nieminen, N. Heckenberg, and H. Rubinsztein-Dunlop, "Orientation of biological cells using plane-polarized Gaussian beam optical tweezers," J. Mod. Opt. **50**, 1581–1590 (2003).
23. D. P. Cherney, T. E. Bridges, and J. M. Harris, "Optical trapping of unilamellar phospholipid vesicles: investigation of the effect of optical forces on the lipid membrane shape by confocal-Raman microscopy," Anal. Chem. **76**, 4920–4928 (2004).
24. S. H. Simpson and S. Hanna, "Optical trapping of spheroidal particles in Gaussian beams," J. Opt. Soc. Am. A **24**, 430–443 (2007).
25. J. Chen, C. Wan, L. Kong, and Q. Zhan, "Experimental generation of complex optical fields for diffraction limited optical focus with purely transverse spin angular momentum," Opt. Express **25**, 8966–8974 (2017).
26. J. Chen, C. Wan, L. Kong, and Q. Zhan, "Tightly focused optical field with controllable photonic spin orientation," Opt. Express **25**, 19517–19528 (2017).
27. A. Balanis, *Antenna Theory: Analysis and Design* (Wiley-Interscience, 2005).
28. B. Richards and E. Wolf, "Electromagnetic diffraction in optical system II. Structure of the image field in an aplanatic system," Proc. R. Soc. London Ser. A Math. Phys. Eng. Sci. **253**, 358–379 (1959).
29. M. Born and E. Wolf, *Principles of Optics: Electromagnetic Theory of Propagation, Interference and Diffraction of Light* (Cambridge University, 1999).
30. M. Neugebauer, T. Bauer, A. Aiello, and P. Banzer, "Measuring the transverse spin density of light," Phys. Rev. Lett. **114**, 063901 (2015).
31. W. Han, Y. Yang, W. Cheng, and Q. Zhan, "Vectorial optical field generator for the creation of arbitrarily complex fields," Opt. Express **21**, 20692–20706 (2013).
32. P. C. Chaumet and M. Nieto-Vesperinas, "Time-averaged total force on a dipolar sphere in an electromagnetic field," Opt. Lett. **25**, 1065–1067 (2000).
33. B. T. Draine, "The discrete-dipole approximation and its application to interstellar graphite grains," Astrophys. J. **333**, 848–872 (1988).
34. L. D. Landau, J. Bell, M. Kearsley, L. Pitaevskii, E. Lifshitz, and J. Sykes, *Electrodynamics of Continuous Media* (Elsevier, 1984).
35. A. Hinojosa-Alvarado and J. C. Gutiérrez-Vega, "Geometrical optics calculation of forces and torques produced by a ringed beam on a prolate spheroid," J. Opt. Soc. Am. B **27**, 1651–1658 (2010).
36. F. G. Mitri, "Optical Bessel beam illumination of a subwavelength prolate gold (Au) spheroid coated by a layer of plasmonic material: radiation force, spin and orbital torques," J. Phys. Commun. **1**, 015001 (2017).
37. K. Svoboda and S. M. Block, "Optical trapping of metallic Rayleigh particles," Opt. Lett. **19**, 930–932 (1994).
38. S. Albaladejo, M. I. Marqués, M. Laroche, and J. J. Sáenz, "Scattering forces from the curl of the spin angular momentum of a light field," Phys. Rev. Lett. **102**, 113602 (2009).
39. M. E. J. Friese, T. A. Nieminen, N. R. Heckenberg, and H. Rubinsztein-Dunlop, "Optical torque controlled by elliptical polarization," Opt. Lett. **23**, 1–3 (1998).
40. H. Polaert, G. Gréhan, and G. Gouesbet, "Forces and torques exerted on a multilayered spherical particle by a focused Gaussian beam," Opt. Commun. **155**, 169–179 (1998).
41. J. W. Liaw, Y. S. Chen, and M. K. Kuo, "Spinning gold nanoparticles driven by circularly polarized light," J. Quant. Spectrosc. Radiat. Transfer **175**, 46–53 (2016).